Nature Communications

https://doi.org/10.1038/s41467-025-67647-y

Article in Press

TMEM65-dependent Ca2+ extrusion safeguards mitochondrial homeostasis

Received: 18 March 2024

Accepted: 4 December 2025

Cite this article as: Vetralla, M., Wischhof, L., Kahsay, A. *et al.* TMEM65-dependent Ca2+ extrusion safeguards mitochondrial homeostasis. *Nat Commun* (2025). https://doi.org/10.1038/s41467-025-67647-y

Massimo Vetralla, Lena Wischhof, Asrat Kahsay, Vanessa Cadenelli, Enzo Scifo, Beijia Xie, Miriana Sbrissa, Maëlle Sandhira Habert, Dan Ehninger, Rosario Rizzuto, Daniele Bano & Diego De Stefani

We are providing an unedited version of this manuscript to give early access to its findings. Before final publication, the manuscript will undergo further editing. Please note there may be errors present which affect the content, and all legal disclaimers apply.

If this paper is publishing under a Transparent Peer Review model then Peer Review reports will publish with the final article.

ARTICLE IN PRESS

© The Author(s) 2025. **Open Access** This article is licensed under a Creative Commons Attribution-NonCommercial-NoDerivatives 4.0 International License, which permits any non-commercial use, sharing, distribution and reproduction in any medium or format, as long as you give appropriate credit to the original author(s) and the source, provide a link to the Creative Commons licence, and indicate if you modified the licensed material. You do not have permission under this licence to share adapted material derived from this article or parts of it. The images or other third party material in this article are included in the article's Creative Commons licence, unless indicated otherwise in a credit line to the material. If material is not included in the article's Creative Commons licence and your intended use is not permitted by statutory regulation or exceeds the permitted use, you will need to obtain permission directly from the copyright holder. To view a copy of this licence, visit http://creativecommons.org/licenses/by-nc-nd/4.0/.

ARTICLE IN PRESS

TMEM65-dependent Ca^{2+} extrusion safeguards mitochondrial homeostasis

Massimo Vetralla[1,4], Lena Wischhof [2,], Asrat Kahsay[1,*], Vanessa Cadenelli[1,5], Enzo Scifo[2], Beijia Xie[2], Miriana Sbrissa[1], Maëlle Sandhira Habert[2], Dan Ehninger[2], Rosario Rizzuto[1,3], Daniele Bano[2], Diego De Stefani[1,3]*

[1]*Department of Biomedical Sciences, University of Padova, Padova, Italy*
[2]*German Center for Neurodegenerative Diseases (DZNE), Bonn, Germany*
[3]*Padua Center for Network Medicine, University of Padova, Padova, Italy*
[4]*Present address: Lonza Group Ltd, Visp, Switzerland*
[5]*Present address: Novartis Institutes for Biomedical Research, Basel, Switzerland*
[*]*These authors contributed equally*

Correspondence:
Diego De Stefani
Department of Biomedical Sciences
University of Padova
Via Ugo Bassi 58B
35131 Padova (PD), Italy
diego.destefani@unipd.it

Keywords: TMEM65, mitochondria, mitochondrial calcium, ion transporters

ARTICLE IN PRESS

ARTICLE IN PRESS

Abstract

The bidirectional transport of Ca^{2+} into and out of mitochondria regulates metabolism, signaling, and cell fate. While influx is mediated by the Mitochondrial Calcium Uniporter (MCU) complex, efflux mechanisms are more diversified, involving Na^+ or H^+ exchange pathways. We here demonstrate that TMEM65 is a fundamental component of the Ca^{2+} efflux machinery of mitochondria. Its overexpression specifically enhances Na^+- and Li^+-dependent mitochondrial Ca^{2+} extrusion. This effect is inhibited by CGP-37157 and does not depends on NCLX, currently considered the bona fide mitochondrial Na^+/Ca^{2+} exchanger. Its downregulation chronically elevates basal $[Ca^{2+}]_{mt}$ and impairs efflux upon stimulation. In *Caenorhabditis elegans*, deletion of TMEM65 homologs compromises embryonic development under mild thermal stress, causing necrotic lesions that are suppressed by genetic inhibition of MCU-1. These findings highlight a molecular component that may be relevant in pathological settings in which excessive mitochondrial Ca^{2+} accumulation critically contribute to degenerative pathways.

Introduction

Calcium (Ca^{2+}) acts as a universal and ubiquitous intracellular messenger, exerting control over every facet of cellular pathophysiology[1]. Such a remarkable versatility relies on the one hand on a large array of dedicated Ca^{2+} binding and/or transporting proteins, and on the other hand on the strictly controlled compartmentalization of $[Ca^{2+}]$ changes. In such a sophisticated framework, mitochondria significantly shape intracellular Ca^{2+} dynamics and downstream Ca^{2+}-dependent pathways. In healthy cells at rest, intramitochondrial $[Ca^{2+}]$ ($[Ca^{2+}]_{mt}$) matches cytoplasmic $[Ca^{2+}]$ ($[Ca^{2+}]_{cyt}$) at approximately 100 nM. Upon cellular stimulation, mitochondria undergo a rapid transient rise in $[Ca^{2+}]_{mt}$ that largely exceed bulk $[Ca^{2+}]_{cyt}$, up to 1 mM in a few cases[2,3]. This marked accumulation of Ca^{2+} is in part due to the highly negative organelle membrane potential (-180 mV), but also to the strategic positioning of mitochondria near Ca^{2+}-releasing channels of the endoplasmic reticulum or the plasma membrane, where local micro/nano-domains of high $[Ca^{2+}]$ are generated[4]. Inside mitochondria, Ca^{2+} acts as a positive modulator of three dehydrogenases (PDH, IDH3 and OGDH), which stimulating oxidative metabolism and eventually ATP synthesis[5]. In pathological conditions, excessive Ca^{2+} accumulation within the organelle matrix (commonly referred to as Ca^{2+} overload) can potentially trigger permeability transition, ultimately leading to membrane permeabilization that may promote the release of pro-death factors[6–8]. Functioning as auxiliary cellular Ca^{2+} reservoirs, mitochondria contribute to buffering intracellular $[Ca^{2+}]$ transients, thereby influencing the spatio-temporal patterns of $[Ca^{2+}]$ oscillations, either within micro/nano-domains or on a bulk scale (e.g., throughout the entire cell)[9]. Consequently, impairment of mitochondrial Ca^{2+} homeostasis has been implicated in the pathogenesis of a variety of human diseases, ranging from neuromuscular diseases to brain injuries[10,11].

From a biophysical perspective, $[Ca^{2+}]_{mt}$ is dynamically determined by the rates of Ca^{2+} influx versus efflux across the IMM. Pioneering investigations conducted in the 1960s and 1970s elucidated the mechanisms underlying this regulation: Ca^{2+} entry into mitochondria is facilitated by an electrogenic uniporter, while Ca^{2+} extrusion occurs through two distinct mechanisms - one dependent on sodium ions (i.e. mediated by a Na^+/Ca^{2+} exchanger) and the other Na^+-independent (i.e. mediated by a H^+/Ca^{2+} exchanger)[12,13]. At the molecular level, mitochondrial Ca^{2+} influx is orchestrated by the MCU complex, whose precise composition varies across tissues and may encompass components such as MCU, MCUb, EMRE, MICU1, MICU2, and MICU3[14]. As to the

efflux, the protein NCLX, encoded by the SLC8B1 gene, has been identified as the mediator of Na^+-dependent Ca^{2+} extrusion[15], whereas two distinct proteins, LETM1[16,17] and TMBIM5[18,19], have been proposed to function as mitochondrial H^+/Ca^{2+} exchangers. Given the breakthrough discoveries of the last years, it is not possible to rule out that other molecular components may contribute to mitochondrial Ca^{2+} transport. Here, we identify TMEM65 as an unexpected, broadly conserved protein that enables Na^+-dependent mitochondrial Ca^{2+} efflux. We found that genetic manipulation of TMEM65 expression causes striking effects on mitochondrial Ca^{2+} homeostasis in cultured cells. Specifically, TMEM65 overexpression effectively suppresses mitochondrial [Ca^{2+}] transients independently of NCLX , while its silencing prevents the decay of the organellar Ca^{2+} rises, resulting in markedly elevated resting $[Ca^{2+}]_{mt}$ levels. Consistent with the prominent contribution of TMEM65 to organelle Ca^{2+} clearance, we show that genetic deletion of *TMEM65* homologues in *Caenorhabditis elegans* causes an overt necrotic phenotype that could be prevented by inhibiting mitochondrial Ca^{2+} influx, thereby pointing out that mitochondrial Ca^{2+} overload is a crucial determinant of cell demise. Since a human subject harboring a homozygous *TMEM65* loss-of-function mutation exhibits a neuromuscular phenotype reminiscent of mitochondrial disease[20], it is reasonable to consider MCU inhibition as a potential therapeutic strategy for conditions characterized by excessive mitochondrial Ca^{2+} accumulation.

Results and discussion

TMEM65 is a conserved protein of the IMM

We previously performed a bioinformatic analysis and identified candidate mitochondrial proteins of the inner membrane with a putative function in Ca^{2+} signaling[21]. Besides MCU, the list contains the recently described mitochondrial H^+/Ca^{2+} exchanger TMBIM5 (also known as GHITM/MICS1). Thus, we sought to further inspect the list of presumed Ca^{2+} transporters using an evolutionary analysis to look for proteins with a conservation profile similar to MCU, and focused on a protein named TMEM65 (Fig 1a). Among these candidates, TMEM65 is a 25 kDa protein with 3 transmembrane domains and a glycine zipper motif that are well conserved in kinetoplastids, green algae (but not in other plants) and metazoan (Fig 1b and Supplementary Fig 1a-b). Mammalian TMEM65 also shows an apparent poly-acidic tail near the C terminus. Although two works proposed TMEM65 as a protein positioned to cardiac sarcolemma[22,23], multiple lines of evidence indicate that TMEM65 is a *bona fide* mitochondrial protein. In this regard, i) TMEM65 expression is not limited to the heart but rather is ubiquitous (highest in the cerebellum, lowest in the liver, Supplementary Fig 1c), ii) sequence analysis of TMEM65 reveals a conserved, prototypical mitochondrial targeting signal at the N-terminal (Fig 1b, predicted MPP-cleaved peptide indicated in cyan), and iii) TMEM65 is present in all high quality mitochondrial datasets based on robust proteomic evidence, including MitoCarta[24], MitoCOP[25] and MitoPhos[26]. To confirm these predictions and assess TMEM65 localization, we cloned, tagged (3xFlag) and expressed human TMEM65 in HeLa cells. Immunoblot analyses show a major band running with high specificity at 20 kDa, in line with the predicted molecular weight of the mature protein after processing by the Mitochondrial Processing Peptidase (MPP). The unprocessed 25 kDa precursor is also detectable upon overexpression (Fig 1c). Immunofluorescence analyses confirm co-localization with the mitochondrial marker SDHA (Fig 1d). To test protein topology across the IMM, we performed Proteinase K (PK) protection assay in isolated mitoplasts. Digestion of intact (but not permeabilized) mitoplasts causes the loss of full-length TMEM65 and the appearance of a smaller fragment, indicating that a significant portion of TMEM65 resides within the matrix (Fig 1e). Of note, the Flag peptide fused at the C-terminus of TMEM65 is lost after PK treatment (Fig

1e), thereby demonstrating that TMEM65 is inserted in the IMM as depicted in Fig 1b. This membrane orientation is also supported by other studies[27], including an independent spatially-resolved proteomic screening that mapped Tyrosine 77 within the matrix (Y77, highlighted in grey in Fig 1b)[28].

TMEM65 expression modulates mitochondrial Ca^{2+} homeostasis

We next tested the role of TMEM65 on mitochondrial Ca^{2+} handling by monitoring $[Ca^{2+}]_{mt}$ in living intact HeLa cells using mitochondrial-targeted genetically-encoded Ca^{2+} indicators (GECI) based on the Ca^{2+}-sensitive bioluminescent protein Aequorin[29]. Control and TMEM65-overexpressing cells were continuously perfused with modified Krebs-Ringer buffer and challenged with 100 μM histamine, an inositol 1,4,5-trisphosphate (IP_3)-generating agonist that elicits Ca^{2+} release from the endoplasmic reticulum, leading to a transient increase of $[Ca^{2+}]$ in both cytoplasm and mitochondria. Interestingly, TMEM65 overexpression robustly inhibits (approximately 80%) the peak of $[Ca^{2+}]_{mt}$ upon cellular stimulation (Fig 2a). Importantly, this effect on mitochondrial Ca^{2+} handling is specific, since no major changes were detected in terms of cytosolic Ca^{2+} dynamics (Supplementary Fig 2a-b) and mitochondrial membrane potential (Supplementary Fig 2c), hence ruling out possible confounding factors. To obtain additional insights into the structure-to-function relationship of TMEM65, we generated a set of mutants by introducing individual substitutions in the most conserved amino acids or by disrupting relevant motifs (i.e. glycine zipper and poly-acidic tail, Supplementary Fig 2d). All TMEM65 variants are expressed at a levels similar or greater compared to wild-type, with the exception of the mutant lacking the transmembrane glycine zipper motif (GZ dead), that completely fail to express at protein level, probably due to an impairment in membrane packing (Supplementary Fig 2e-f)[30]. We evaluated histamine-induced $[Ca^{2+}]_{mt}$ peaks in cells expressing wild-type (wt) or mutant TMEM65. Our data indicate that D132, D167, G170 and E178 are required for TMEM65 activity, while G140L and Q195E mutants are very similar to wild type (Supplementary Fig 2g-h). The TMEM65 mutant lacking the poly-acidic tail still retain some effect, although to a lower extent when compared to wt. Surprisingly, the E144Q mutant shows even stronger effect than the wt. None of these mutants affects the expression of the primary mitochondrial Ca^{2+} influx and efflux transporters (Supplementary Fig 2f). Overall, these data suggest a clear, specific involvement of TMEM65 in the regulation of mitochondrial Ca^{2+} handling.

We next evaluated the effect of TMEM65 downregulation on organelle Ca^{2+} dynamics by testing different synthetic unmodified siRNAs. When agonist-induced peak $[Ca^{2+}]_{mt}$ values were compared, we obtained inconsistent results among siRNA sequences (Supplementary Fig 3a-b) despite comparable efficiency in reducing TMEM65 protein level (Supplementary Fig 3e), an outcome likely due to off-target effects. To enhance specificity, we used endoribonuclease-prepared siRNAs (esiRNA)[31]. This approach reveals increased $[Ca^{2+}]_{mt}$ peak upon specific downregulation of TMEM65 (Fig 2a-b). More importantly, in addition to the effect on maximal $[Ca^{2+}]_{mt}$ values, TMEM65 silencing alters the kinetic profile of $[Ca^{2+}]_{mt}$ transients. In particular, a delayed Ca^{2+} clearance after the peak is noticeable, an indication of impaired mitochondrial Ca^{2+} extrusion. To better appreciate this effect, we re-analyzed all Ca^{2+} traces by normalizing $[Ca^{2+}]_{mt}$ on peak $[Ca^{2+}]$ (Supplementary Fig 3c). The slope of the resulting trace is thus proportional to mitochondrial Ca^{2+} efflux rate (Supplementary Fig 3d). This analysis clearly reveals that TMEM65 overexpression enhances mitochondrial Ca^{2+} extrusion (notwithstanding lower $[Ca^{2+}]_{mt}$ peak), while its silencing elicits the opposite effect. Remarkably, all tested siRNAs consistently decreased mitochondrial Ca^{2+} efflux, irrespective of their wavering effect on peak $[Ca^{2+}]_{mt}$ (Supplementary Fig 3a-d). Furthermore, expression analyses of the two main mitochondrial Ca^{2+} transporters

(MCU for the influx, NCLX for the efflux) revealed no significant changes (Supplementary Fig 3f). Due to the lack of specificity of the commercial antibodies tested, NCLX protein levels could not be reliably assessed (Supplementary Fig 4). Altogether, these data suggest an involvement of TMEM65 in mitochondrial Ca^{2+} efflux rather than in influx. To further substantiate our data, we evaluated mitochondrial Ca^{2+} dynamics using a GFP-based GECI, the mitoGCaMP6 probe, that also allows the more precise quantification of baseline $[Ca^{2+}]_{mt}$ and extrusion kinetics[32]. Compared to controls, both overexpression and downregulation of TMEM65 alter mitochondrial Ca^{2+} dynamics, further supporting that TMEM65 is a key regulator of mitochondrial Ca^{2+} efflux (Fig 2c). Specifically, TMEM65 overexpression causes a negligible decrease of resting Ca^{2+}, a histamine induced upstroke similar to control, at least in the initial phase, but most evidently, a steep return to baseline after the peak (Fig 2c). Conversely, TMEM65-silenced cells show chronically elevated resting matrix Ca^{2+} levels, and histamine-induced $[Ca^{2+}]$ elevations that last over several minutes (Fig 2c-d). Altogether, our detailed analyses of mitochondrial Ca^{2+} dynamics uncover a prominent role of TMEM65 in controlling mitochondrial Ca^{2+} efflux.

TMEM65 mediates Na^+-dependent mitochondrial Ca^{2+} efflux

We next explore the mechanism underlying TMEM65 effect on mitochondrial Ca^{2+}. It is known that experiments carried out in intact cells have the benefit of examining mitochondria in their native environment. However, these experimental settings suffer from two main drawbacks. Firstly, mitochondrial Ca^{2+} influx and efflux constantly coexist, thus preventing the genuine segregation of the two phenomena. Secondly, efflux relies on two concurrent but separate mechanisms, one Na^+-dependent and the other Na^+-independent. To overcome these limitations, we performed $[Ca^{2+}]_{mt}$ measurements in digitonin-permeabilized cells, where mitochondria can be exposed to buffers with defined ionic composition. In this experimental setup, mitochondrial Ca^{2+} uptake was initiated by perfusing mitochondria of plasma-membrane permeabilized cells with an intracellular-like buffer containing fixed $[Ca^{2+}]$, until a plateau $[Ca^{2+}]_{mt}$ is reached (i.e. when influx rate equals efflux rate). Then, MCU inhibitor Ruthenium Red (RuR) was added to block the influx, resulting in a progressive decrease of $[Ca^{2+}]_{mt}$. The rate of this decrease represents a reliable measurement of mitochondrial Ca^{2+} efflux. Perfusion with Na^+-free buffer allows the evaluation of organelle Na^+-independent efflux, while incorporation of 10 mM NaCl in the RuR-containing buffer enhances mitochondrial Ca^{2+} extrusion, thereby enabling the quantification of Na^+-dependent efflux. Li^+ can also be used as Na^+ surrogate, although less effective[33]. Using this approach, we found that both TMEM65 overexpression and downregulation showed no effects on mitochondrial Ca^{2+} influx or Na^+-independent efflux. Rather, TMEM65 overexpression greatly enhanced Na^+- and Li^+-dependent mitochondrial Ca^{2+} efflux. Indeed, its silencing blunted the Na^+-dependent component of organellar Ca^{2+} extrusion (Fig 3a-d, Supplementary Fig 5a-b). To further support this finding, we took advantage of the specific pharmacological inhibitor of mitochondria Na^+/Ca^{2+} exchange, the benzothiazepine CGP-37157[34]. This compound causes an increase in agonist-induced $[Ca^{2+}]_{mt}$ peaks in control cells due to the inhibition of organelle Ca^{2+} efflux[35]. Strikingly, CGP-37157 was able to abrogate the effect elicited by TMEM65 overexpression, restoring normal mitochondrial Ca^{2+} dynamics (Fig 3 e-g). Overall, these results indicate that i) mitochondrial Ca^{2+} efflux strongly counteracts both in resting conditions and in all phases of agonist-evoked responses the action of MCU and ii) TMEM65 is a key contributor to the process of Na^+-dependent mitochondrial Ca^{2+} efflux.

TMEM65 acts independently of NCLX

The potential relationship between TMEM65 and the mitochondrial Na^+/Ca^{2+} exchanger NCLX warrants investigation. Although the TMEM65 sequence shows no similarity to that of known

exchangers—suggesting a possible modulatory role—functional analyses indicate that its overexpression and silencing strongly enhance and suppress, respectively, Na^+-dependent mitochondrial Ca^{2+} extrusion. This positions TMEM65 as the molecular rate-limiting factor for the process. Conflicting reports in the literature[36,37] prompted us to test whether TMEM65 activity depends on the sole characterized mitochondrial Na^+/Ca^{2+} exchanger. In cells acutely silenced for NCLX (Supplementary Fig 3f), TMEM65 overexpression markedly reduced $[Ca^{2+}]_{mt}$ peaks (Fig 4a–b), indicating functional independence. To rule out compensation from residual NCLX, we generated both polyclonal and monoclonal NCLX knockout (KO) cell lines. In a consistent manner, TMEM65 overexpression lowered agonist-induced $[Ca^{2+}]$ peaks (Fig 4c) and increased Ca^{2+} extrusion rates in intact (Fig 4e) and permeabilized cells (Fig 4f–g), confirming that NCLX is dispensable for TMEM65 function. In the same models, the Na^+/Ca^{2+} exchange inhibitor CGP-37157 not only abrogated the stimulatory effect of TMEM65 overexpression (Fig 4b) but also remained active in NCLX-silenced and NCLX-KO cells (Fig 4b; Supplementary Fig 6). Together, these results demonstrate that TMEM65 operates independently of NCLX, and indicate TMEM65 as one of the molecular targets of CGP-37157.

TMEM65 deficiency causes necrotic lesions *in vivo* in *C. elegans*

To better understand the physiological relevance of TMEM65 *in vivo*, we decided to employ the nematode *Caenorhabditis elegans*. Based on protein alignment (BLAST) using human TMEM65 as a query, we found that *C33H5.19/tag-321* and *C03B8.3* genes encode two homologs (here referred to also as CeTMEM65-1 and CeTMEM65-2, respectively) (Fig 5a, Supplementary Fig 7a-c), one of which (TAG-321) with a higher percent identity and a predicted AlphaFold 3D structure relatively similar to the human protein variant (Fig 5b). First, we tested the expression and functionality of CeTMEM65 in mammalian cells. Western blot shows that CeTMEM65-1 is efficiently expressed also in HeLa cells, while CeTMEM65-2 fails to be detected, probably due to instability of the protein at 37°C (Supplementary Fig 7d). In terms of activity, the effect of CeTMEM65-1 on mitochondrial Ca^{2+} handling is comparable to its human counterpart, indicating that their biochemical function is maintained through evolution (Supplementary Fig 7e). Next, we performed CRISPR/Cas9 gene editing and generated deletions of the promoters and exons within *tag-321* and *C03B8.3* genes. Although both *tag-321(bon103)* and *C03B8.3(bon104)* were *(null)* alleles (Supplementary Fig 7f), homozygous mutants did not display any obvious difference compared to wt (N2) nematodes at normal growth conditions (20°C, *E. coli* B-type strain as a bacterial food). When we generated *C03B8.3;tag-321* double *(null)* mutants, we observed a significant reduction of hatched larvae compared to wt, *tag-321(bon103)* and *C03B8.3(bon104)* mutants at 20°C (Fig 5c). Lifespan assays at 20°C showed no differences between wt and mutant nematodes, whereas there was a trend toward a minor decreased median lifespan for *CeTMEM65* single and double mutants compared to wt at 25°C (Fig 5d-e and Supplementary tables ST1-3). Intriguingly, while at 20°C we could find larvae in plates from wt and *CeTMEM65* single mutants, at 25°C the large majority of *C03B8.3;tag-321(null)* mutant animals laid eggs that did not hatch. Motivated by this intriguing observation, we decided to assess the number of larvae that could develop and survive at 25°C (Fig 5f). Compared to wild type animals, only ~5% of all *C03B8.3(bon104);tag-321(bon103)* mutants hatched (Fig 5g), with most of the degenerating embryos at gastrula/comma stage showing large vacuoles (Fig 5h). Of note, *C03B8.3(null)* mutants had a hatching rate similar to wt, whereas *tag-321 (null)* animals showed a modest, although significant increased number of larvae that could hatch at 25°C (Fig 5g). Given the resemblance of the large vacuoles to necrotic structures, we reasoned that *mcu-1(lof)* and consequent inhibition of mitochondrial Ca^{2+} influx would restore normal hatching of *CeTMEM65(null)* mutants at 25°C

(Fig 5i). We first attempted to generate *C03B8.3;mcu-1;tag-321* triple mutants using the already existing alleles. However, since *mcu-1* and *tag-321* genes are both on chromosome IV at a very close distance (less than 1 cM), we could not introduce the *mcu-1(ju1154)* allele into the existing *C03B8.3(null);tag-321(null)* background. To overcome this problem, we performed another gene editing in *mcu-1(ju1154)* animals and generated an equivalent lesion within *tag-321* gene. DNA sequencing confirmed that the newly generated *tag-321(bon105)* allele was matching the previous *tag-321(bon103)* mutation (Supplementary Fig 7g-h). We backcrossed the new strain, generated *C03B8.3(bon104);mcu-1(ju1154);tag-321(bon105)* triple mutants and assessed animal hatching. Remarkably, we found that *mcu-1(lof)* completely suppressed the degeneration of *C03B8.3;tag-321* double mutant embryos at 25°C (Fig 5j-k), indicating a genetic interaction between *mcu*-1 and *CeTMEM65* and further supporting the prominent role of TMEM65 as a key regulator of mitochondrial Ca^{2+} efflux. To confirm our findings and rule out any eventual egg-laying defects of individual hermaphrodites, we performed a population-based hatching assay in which eggs were extracted from hundreds of gravid young adult hermaphrodites and plated on bacteria-seeded NGM plates (Fig 5l). Consistent with our previous findings, while the large majority of *C03B8.3;tag-321* double mutant embryos did not hatch at 25°C, *C03B8.3(bon104);mcu-1(ju1154);tag-321(bon105)* triple mutants hatched and developed at a comparable rate of wt animals (Fig 5m). Using this experimental paradigm, *CeTMEM65* single mutants did not show any difference compared to wt (Fig 5n).). Of note, the hatching rate of *mcu-1(ju1154)* was comparable to wt (Supplementary Fig 7i). Together, our *in vivo* evidence demonstrates that TMEM65 deficiency may facilitate mitochondrial Ca^{2+} overload when cells are exposed to environmental challenges (e.g., restrictive temperatures) that may induce degenerative processes (necrosis-like death). Finally, we tested whether NCLX loss of function could recapitulate the same phenotype observed in *C03B8.3;tag-321* double mutants (Fig 5o). It was previously suggested that NCX-9 is the putative NCLX-type Na^+/Ca^{2+} exchanger in *C. elegans*[38]. Using two *ncx-9(lof)* alleles, we carried out our population-based hatching assay and found that NCX-9 loss did not alter *C. elegans* hatching at 25°C (Fig 5p). Although we cannot rule out that other NCLX-type exchangers may compensate for NCX-9 deficiency and/or contribute to mitochondrial Ca^{2+} extrusion, our data report unique developmental defects associated with CeTMEM65 dysfunction that causes death in an MCU-dependent manner.

In conclusion, we confirmed the critical function of TMEM65 in regulating mitochondrial Ca^{2+} fluxes. TMEM65 is both sufficient to enhance Na^+-dependent mitochondrial Ca^{2+} extrusion, as shown by overexpression experiments, and necessary to prevent organellar Ca^{2+} overload, as evidenced by siRNA-mediated knockdown *in vitro* and *in vivo* in in *C. elegans* mutants. Importantly, TMEM65 activity does not require the presence of NCLX, which has long been considered the *bona fide* mitochondrial Na^+/Ca^{2+} exchanger. This unexpected result aligns with recent data showing that TMEM65 alone, when reconstituted in liposomes, exhibits intrinsic Ca^{2+} transport activity. These findings establish TMEM65 as an autonomous molecular entity with Na^+/Ca^{2+} exchange capacity and prompt a critical reassessment of the genuine contribution of NCLX to mitochondrial Ca^{2+} homeostasis. More importantly, our findings also shed light on the pathogenic mechanism underlying a reported human neuromuscular syndrome associated with TMEM65 deficiency, where mitochondrial dysfunction emerges as a central feature. Based on our *in vivo* experimental paradigm, MCU inhibition may represent a viable strategy to mitigate the deleterious effects of TMEM65 loss. Considering that excessive mitochondrial Ca^{2+} accumulation is implicated in numerous diseases, our work lays the foundation for therapeutic approaches aimed at restoring mitochondrial Ca^{2+} balance.

Methods

Chemicals, cell culture and transfection

All chemicals were purchased from Sigma-Aldrich, unless otherwise specified. All the experiments were performed in HeLa cells (ATCC Number: CCL-2) cultured in Dulbecco's modified Eagle's medium (DMEM) (Gibco #41966052, Thermo Fisher Scientific), supplemented with 10% fetal bovine serum (FBS) (Thermo Fisher Scientific), containing penicillin (100 U/ml) and streptomycin (100μg/ml) (Euroclone). NCLX-KO cells were purchased from SyntheGo (now EditCo). Knockout cells were generated using Crispr-Cas9 technology by targeting exon 2 of the SLC8B1 gene using the following guide RNA sequence: ACACCUGAAGCUGGAAACUG. When needed, cells were seeded on either glass coverslips (onto 13- or 24-mm in diameter) or 96-well plates and allowed grow to 50-80% confluence before transfection. Transfection of siRNA was performed using RNAiMAX (Thermo Fisher Scientific) according to manufacturer's instructions. Transfection of plasmid DNA was performed using polyethylenimine (PEI MAX, Polysciences).

Plasmids and siRNAs

Plasmids encoding C-term 3xFlag tagged human TMEM65 (NM_194291.2), *C. elegans* TAG-321 (NM_068883.5), and *C. elegans* C03B8.3 (NM_066278.5) were purchased from VectorBuilder. Untagged human TMEM65 was amplified using the following primer: fw 5'-ATTAGCTAGCACCACCATGTCCCGGCTG-3', rv 5'-ATTAGAATTCTTAACTTTTCGTTTCCAGTTTTTCATCTTCTTC-3'. The PCR fragment was cloned into pcDNA3.1 (Thermo Fisher Scientific) using NheI and BamHI sites.

Mutagenesis was performed using In-Fusion cloning (Takara) using the following primer pairs:

D132N	fw: 5'-CTTTTTGAATAATGCAATTATGATTGTTGCTGG
	rv: 5'-GCATTATTCAAAAAGCCAAACCCTATGAAAGG
G140L	fw: 5'-TGTTGCTTTAACCCATATTGAAATGTCTATTGG
	rv: 5'-TGGGTTAAAGCAACAATCATAATTGCATTATCC
E144Q	fw: 5'-CCATATTCAAATGTCTATTGGAATTATTTTGGGAA
	rv: 5'-GACATTTGAATATGGGTTCCAGCAACAATCA
D167N	fw: 5'-TGTGTCAAACCTAGCTGGACTTGGACTTGC
	rv: 5'-GCTAGGTTTGACACAAGATTTCCCAAAGCAGC
G170L	fw: 5'-TCTAGCTCTTCTTGGACTTGCAGGCTACG
	rv: 5'-CCAAGAAGAGCTAGATCTGACACAAGATTTCCC
E178Q	fw: 5'-CTACGTTCAAGCATTGGCTTCCAGGTTAGG
	rv: 5'-AATGCTTGAACGTAGCCTGCAAGTCC
Q195E	fw: 5'-ACCAAAGGAAGTTGACATGTGGCAAACACGTC
	rv: 5'-TCAACTTCCTTTGGTGTGAGATCAGGAATTGAC
ΔPolyAc	fw: 5'-GAGGAGGTAAACTGGAAACGAAAAGTGACTAC
	rv: 5'-CCAGTTTACCTCCTCCAAAGAAAATTAAAGG

GZ dead	fw: 5'-TGCTGTGACTATTGCATGCATTCTAGCTATGTTTCCTTTAATTTTCTTTGGAG
	rv: 5'-GCAATAGTCACAGCAACAGCTTTTGCCAAATGTGTACTAAGACGTGTTTG

All constructs were verified by Sanger sequencing.

The following siRNAs were purchased from Sigma-Aldrich: esiRNA-RLuc (cat no EHURLUC), esiRNA-TMEM65 (cat no EHU042431), esiRNA-SLC8B1 (cat no EHU154091), siRNA Universal Negative Control #2 (cat no SIC002), siRNA-TMEM65#1 (cat no SASI_Hs01_00147974), siRNA-TMEM65#2 (cat no SASI_Hs02_00371420), siRNA-TMEM65#3 (cat no SASI_Hs01_00147977), siRNA-TMEM65#4 (SASI_Hs01_00147978).

Antibodies, SDS-PAGE and Western blot

Cells were lysed in RIPA buffer (150 mM NaCl, 25 mM Tris-Cl pH 8, 1 mM EGTA-Tris, 1% Triton X-100, 0.5% sodium deoxycholate and 0.1% SDS) supplemented with Complete EDTA-free protease inhibitor mixture (Roche Applied Science) and PhosStop (Roche Applied Science) for 30 minutes on ice. Crude extracts were centrifuged 15000 *g* for 10 minutes to remove debris, and proteins in the supernatant were quantified using the BCA Protein Assay Kit (Pierce). Approximately 30 μg of proteins were dissolved in LDS sample buffer (Life Technologies) supplemented with 10 mM dithiothreitol, heated for 5 minutes at 95°C and loaded on 4-12% Bis-Tris NuPage gels (Thermo Fisher Scientific). After electrophoretic separation, proteins were transferred onto nitrocellulose membranes by semidry transfer (BioRad). Membranes were blocked for 1 hour at RT with 5% non-fat dry milk in TBS-T (50 mM Trizma, 150 mM NaCl and 0.1% Tween) and probed with the indicated primary antibodies over night at 4°C. Isotype matched, horseradish peroxidase-conjugated secondary antibodies (1:10000, BioRad) were used followed by detection by chemiluminescence (SuperSignal Pico, Pierce). The following primary antibodies were used: anti-GRP75 (1:1000, SCBT sc-133137), anti-TMEM65 (1:1000, Thermo Fisher Scientific PA5-112762), anti-Flag (1:1000, Cell Signaling #2368), anti SDHA (1:1000, Cell Signaling #5839), anti-PDHA1 (1:1000, Cell Signaling #2784), and anti-MITOK (1:10000, Sigma HPA010980), anti-NCLX (Proteintech 21430-1-AP, Thermo PA5-114330 and Abcam ab83551). Western blots are representative of at least three independent preparations. For Western blot analyses of *C. elegans* samples, adult animals were collected in water and snap-frozen in liquid nitrogen. *C. elegans* pellets were then sonicated in RIPA buffer supplemented with protease and phosphatase inhibitors (Roche). Lysates were centrifuged as described above and protein concentrations were quantified via Bradford assay (Sigma-Aldrich). Approximately 20-30 μg of protein was resolved on 8% polyacrylamide gels and transferred onto nitrocellulose membranes using semi-dry Trans-Blot Turbo™ (Bio-Rad). Following antibody incubation (anti-GFP, 1:1000, Roche #118144600001), membranes were developed in ECL and imaged using the Chemidoc imaging system (Bio-Rad). Uncropped images of Western blots used for the assembly of final figures are provided as Supplementary Figures.

RNA extraction, reverse transcription, and qPCR

Total RNA was extracted from HeLa cells using the RNeasy Plus Micro Kit (Qiagen) according to the manufacturer's instructions. RNA concentration was quantified using a NanoDrop spectrophotometer (Thermo Fisher Scientific). For cDNA synthesis, 1 μg of RNA from each sample was reverse transcribed using the SuperScript II cDNA synthesis kit (Thermo Fisher Scientific), following the manufacturer's protocol. Oligo(dT)12–18 primer (Thermo Fisher Scientific) was used for first-strand cDNA synthesis, along with dNTPs (deoxynucleotide triphosphates, Thermo Fisher Scientific) and reverse transcriptase.

The resulting cDNA was analyzed by quantitative PCR (qPCR) using TaqMan probe-based chemistry to assess relative gene expression levels. qPCR reactions were carried out in 384-well plates using TaqMan Gene Expression Master Mix (Applied Biosystems) and gene-specific TaqMan probes. Amplification was performed on a QuantStudio 5 real-time PCR system (Thermo Fisher Scientific) under standard cycling conditions. Relative gene expression was calculated using the ΔΔCt method, with *TOMM20* or *ACTIN* serving as the endogenous control, as indicated in figure legend. The following probes were used: TOMM20-VIC (cat no Hs00740685_sH), ACTB-VIC (cat no Hs01060665_g1), MCU-FAM (cat no Hs00293548_m1), MCU-FAM (cat no Hs00293548_m1), SLC8B1-FAM (cat no Hs00905331_m1).

Bioinformatic analyses

To evaluate conservation profiles of MCU and TMEM65, reference proteomes of eukaryotic species were retrieved from Uniprot as fasta files (Release 2022_02, 25-May-2022). Only species containing at least 3000 entries in main (canonical) set were considered for further analysis. Homology searches were performed using phmmer (HMMER version 3.3.2)[39]. Human MCU and TMEM65 protein sequences were used as input against reference proteomes using BLOSUM62 as scoring matrix. Hits with an E-value below 0.05 were considered as homologs. Multiple sequence alignments (ClustalW) and phylogenetic trees (RAxML) were performed using MegAlign Pro (DNASTAR version 17.3.1). Visualization of protein topology was generated using Protter[40]. Prediction of transmembrane domains was performed using TMHMM[41]. The presence of mitochondrial targeting peptides was evaluated using TPP3[42], MitoFates[43] and TargetP[44]. Highly conserved amino acids were identified by performing a multiple sequence alignment across selected species and selecting residues with a sequence logo score ≥ 3.5 bits (log_2-scaled; maximum score = 4.3 bits for 20 amino acids). To evaluate tissue expression of TMEM65, RNA-seq expression values (TPM) were retrieved from GTEx portal[45]. To normalize to mitochondrial abundance, we calculated the average expression of a large subset of broadly expressed mitochondrial proteins, and normalized TMEM65 expression to these values.

Mitochondrial isolation and proteinase K protection assay

Mitochondria were isolated from HeLa cells through differential centrifugation as previously described[46]. Mitoplasts were obtained through osmotic swelling by incubating mitochondrial fraction in 20 mM Tris-Cl pH 7.4 for 20 minutes on ice. An equal amount of mitoplasts was treated with proteinase K (100 µg/ml) at room temperature for the indicated time and the proteolytic reaction was quenched by PMSF addition. Samples were then loaded on SDS-PAGE and processed for Western blot as described above. Results are representative of at least three different proteolytic reactions.

Immunofluorescence and confocal imaging

HeLa cells expressing TMEM65-3xFlag were grown on 24 mm coverslips until 50% confluence. Cells were then washed with PBS, fixed in 4% formaldehyde for 10 minutes and quenched with 50 mM NH_4Cl in PBS. Cells were permeabilized for 10 minutes with 0.1% Triton X-100 in PBS and blocked in PBS containing 2% BSA for 1 hour. Cells were then incubated with primary antibodies for 3 hours at room temperature and washed 3 times with 0.1% Triton X-100 in PBS. The following primary antibodies were used: anti-SDHA (1:100, Cell Signaling #5839), anti-Flag (1:100, Cell Signaling #2368), The appropriate isotype matched AlexaFluor-conjugated secondary antibodies (1:500, Thermo Fisher Scientific) were incubated for 1 hour at RT and coverslips were mounted with ProLong Diamond Antifade reagent (Thermo Fisher Scientific). Images were

acquired on a Leica TCS-SP5-II-RS-WLL equipped with a 100x, 1.4N.A. Plan-apochromat objective. AlexaFluor488 was excited by the 488 nm laser line and images were collected in the 495-535 nm range. AlexaFluor555 was sequentially excited with the 543 nm laser line and signal was collected in the 555-600 nm range. Pixel size was set below 100 nm to meet the Nyquist criterion. For each image, a z-stack of the whole cell was acquired, with a step size of 130 nm. Images are presented as maximum projections of the whole stack and were generated using the Fiji image processing package based on ImageJ[47]. Images are representative of at least three independent transfections.

[Ca^{2+}] measurements

For experiments in intact cells using bioluminescent probes, HeLa cells were grown on 96-well plates and cotransfected with an Aequorin based probe[48,49] together with the indicated constructs. siRNAs were delivered through RNAiMAX-mediated reverse transfection 72 hours before experiments. Plasmids were delivered through PEI-mediated forward transfection 36/48 hours before experiments. Untargeted siRNA (esiRNA-RLuc or universal negative siRNA) and/or pcDNA3.1 were used as controls. For aequorin reconstitution, cells were incubated for 1 hour at 37°C with 5 μM coelenterazine in KRB (Krebs-Ringer modified buffer: 125 mM NaCl, 5 mM KCl, 1 mM Na_3PO_4, 1 mM $MgSO_4$, 5.5 mM glucose, 20 mM HEPES, pH 7.4) supplemented with 1 mM $CaCl_2$. After reconstitution, cells were washed and placed in 70 μl of KRB and luminescence was recorded on a PerkinElmer Envision plate reader equipped with a two-injector unit. Each well was monitored for 50 seconds during which histamine was first injected (final concentration is 100 μM) to activate calcium transients, and then a hypotonic, Ca^{2+}-rich, digitonin-containing solution was added to discharge the remaining aequorin pool. Output data were analyzed and calibrated with a custom made macro-enabled Excel workbook. Where indicated, cells were pre-treated with either vehicle (DMSO) or 20 μM CGP-37157 (Tocris Bioscience).

For experiments in permeabilized cells using bioluminescent probes, HeLa cells were grown on 13 mm round glass coverslips at 50-80% confluence and cotransfected with a low-affinity mitochondrial-targeted aequorin-based probe together with the indicated constructs. For aequorin reconstitution, cells were incubated for 1-2 hours at 37 °C with 5 μM coelenterazine in KRB supplemented with 1 mM $CaCl_2$ and then transferred to the perfusion chamber of a custom-built luminometer[49,50]. Experiments in permeabilized cells were performed in an intracellular-like buffer (IB: 130 mM KCl, 2 mM K_2HPO_4, 5mM glutamic acid, 2 mM malic acid, 1 mM $MgCl_2$, 20 mM HEPES, pH 7.0), supplemented with additional 10 mM KCl, 10 mM NaCl or 10 mM LiCl as specified. Plasma membrane was permeabilized by perfusing cells for 1 min with 100 μM digitonin dissolved in IB containing 500 μM EGTA. Mitochondrial Ca^{2+} uptake in permeabilized cells was initiated by perfusing IB containing 5 μM Ca^{2+}, and influx was blocked by adding 10 μM ruthenium red (RuR). The experiments were terminated by lysing the cells with 100 μM digitonin in a hypotonic Ca^{2+}-rich solution (10 mM $CaCl_2$ in H_2O), thus discharging the remaining aequorin pool. The light signal was collected and calibrated into [Ca^{2+}] values by an algorithm based on the Ca^{2+} response curve of aequorin at physiological conditions of pH, [Mg^{2+}] and ionic strength[51,52].

For experiments in intact cells using fluorescent probes, HeLa cells were grown on 24 mm round glass coverslips at 30-50% confluence and cotransfected with mitoGCaMP6 together with the indicated constructs. Cells were transferred to an imaging chamber and incubated in KRB supplemented with 1 mM $CaCl_2$. Images were acquired on an Olympus IX-73 microscope equipped with a 40x/1.3 N.A. oil-immersion semiapochromat objective (UPLFLN40XO).

Excitation light was selected with a Deltaram V high speed monochromator (Photon Technology International) equipped with a 75W Xenon Arc lamp. MitoGCaMP6 emission was collected through a 525/50 filter (Chroma) mounted on an OptoSpin25 wheel (Cairn research). Images were captured with a Kinetix22 sCMOS camera (Photometrics). The system is controlled by Metamorph 7.10 (Molecular devices) and was assembled by Crisel Instruments. MitoGCaMP6 was used in excitation ratiometric mode, where cells are alternatively illuminated every second at 485 and 410 nm[32]. Typical exposure time was 100 milliseconds. After background correction, 485/410 fluorescence ratio was calculated for each cell. Where indicated, 100 μM histamine was added, followed by addition of 3 μM ionomycin and 5 mM $CaCl_2$ to check for homogenous probe saturation. Analysis was performed with the Fiji distribution of ImageJ[47]. Data are presented as fluorescence ratio (R, 485/410 nm), and each data point represents one coverslip (containing approximately 1 to 5 individual cells).

$\Delta\Psi_m$ measurements

The measurement of mitochondrial membrane potential is based on the distribution of the mitochondrion-selective lipophilic cation dye tetramethylrhodamine, methyl ester (TMRM, Thermo Fisher Scientific). Cells were loaded with 20 nM TMRM for 30 minutes at 37°C and then transferred to the imaging system. Images were acquired on a Zeiss Axiovert 200 microscope equipped with a 40x/1.3 N.A. PlanFluor objective. Excitation was performed with a Deltaram V high speed monochromator (Photon Technology International) equipped with a 75W Xenon Arc lamp. Images were captured with a Evolve 512 Delta EMCCD (Photometrics). The system is controlled by Metamorph 7.5 and was assembled by Crisel Instruments. TMRM excitation was performed at 560 nm and emission was collected through a 590–650 nm bandpass filter. On each coverslips images of 5 random fields were acquired with a fixed 200 milliseconds exposure time. At the end of each experiment, 10μM CCCP was added to collapse $\Delta\Psi_m$. data are presented as average background-corrected fluorescence in resting conditions. Data were obtained from at least three independent preparations. All analyses were performed with the Fiji distribution of ImageJ.

Caenorhabditis elegans strains and maintenance

Nematode cultures were maintained at 20ºC unless differently stated. *C. elegans* was grown on nematode growth media (NGM) plates seeded with a bacterial lawn of OP50 *E. coli* following standard culture methods. The following strains were used in this study: wild type N2 (Bristol), BAN544 *tag-321(bon103)IV*, BAN545 *C03B8.3(bon104)III*, BAN547 *C03B8.3(bon104)III;tag-321(bon103)IV*, BAN580 *C03B8.3(bon104)III;mcu-1(ju1154)IV;tag-321(bon105)IV*, CZ19982 *mcu-1(ju1154)IV*. We are grateful to Dr. Damien M. O'Halloran (Institute for Neuroscience, George Washington University, Washington, D. C, USA) for kindly providing *ncx-9(gk234237)* and *ncx-9(gk773708).* Some strains were provided by the CGC, which is funded by NIH Office of Research Infrastructure Programs (P40 OD010440).

CRISPR/Cas9 gene editing

Young adult *C. elegans* hermaphrodites were injected with customized injection mix of Cas9 protein (pre-complexed with sgRNAs), target-specific sgRNAs, target donor homology repair template (ssODN) (InVivo Biosystem, Eugene, Oregon, USA) and a plasmid encoding *[myo-2p::GFP]*. F1 offspring were screened for GFP expression in the pharynx, while F2 were genotyped using specific oligonucleotides upstream and downstream the expected deletions. DNA sequencing was used to confirm the mutation. Selected positive mutants were backcrossed at least five times with wt (N2) males.

ARTICLE IN PRESS

DIC microscopy

Eggs from adult nematodes were extracted via bleaching, washed twice with water and then transferred onto glass slides. Images were acquired with an EPI-SCOPE1 Apotome microscope equipped with a 63x oil immersion objective (Zeiss).

Hatching assays

Two independent experimental paradigms were used to assess hatching of larvae. In the first one, animals were grown at 20°C, collected at adulthood and bleached with a hypochlorite solution. The extracted eggs were transferred onto bacteria-seeded NGM plates and incubated at either 20°C (for maintenance) or 25°C. Individual young adults were then transferred on freshly bacteria-seeded plates and the hatched progeny was quantified over time (up to 48 hours). For each experiment, between 8 and 15 young adult nematodes per genotype were used. The second hatching assay was a population-based analysis. Animals were grown at 20°C, collected at adulthood and bleached with a hypochlorite solution. Eggs were plated in freshly prepared bacteria-seed plates and transferred at 25°C until hatched animals reached adulthood. Then, synchronized gravid hermaphrodites were collected and bleached with a hypochlorite solution. The extracted eggs were seeded on plates, counted and incubated at 25°C. Hatched larvae were quantified using a stereomicroscope.

Lifespan assay

Gravid adult animals grown at 20°C were collected and bleached using a NaClO/NaOH solution to extract eggs. Synchronized populations were then placed in an incubator at either 20°C or at 25°C, according to the experimental paradigm. Animals were transferred every 2 days and scored at least every other day for touch-provoked movement until death. Animals that died abnormally (e.g., internal hatching, vulva protrusions) were scored as censored. Survival curves were generated using GraphPad Prism software (GraphPad Software Inc., San Diego, USA).

Statistics & Reproducibility

No statistical method was used to predetermine sample size. All experiments were repeated independently at least 3 times with similar results. For the analysis of $[Ca^{2+}]$ dynamics, representative traces are shown together with bar graphs. No data were excluded from the analyses. Experiments were not randomized, and investigators were not blinded to allocation during experiments or outcome assessment. Bar graphs display mean ± standard deviation (s.d.), with individual data points represented by dots unless otherwise indicated. Variance was assessed using one-way, two-way, or three-way ANOVA, as specified in the figure legends. Comparisons between two groups were performed using unpaired two-sample t-tests. For multiple comparisons, Holm–Šidák post hoc tests were applied. Where applicable, raw data and exact p-values are provided in the source data tables. All statistical analyses were conducted using OriginPro (OriginLab), Prism (GraphPad), or Excel (Microsoft).

ARTICLE IN PRESS

Data Availability

Additional unprocessed and processed data supporting the findings are available in the Supplementary Information or Source Data files.

Code Availability

No custom code or mathematical algorithms were used in this study. All analyses were conducted using established methods and standard software, as indicated in the “Methods” section.

ARTICLE IN PRESS

ARTICLE IN PRESS

References

1. Berridge, M. J., Lipp, P. & Bootman, M. D. The versatility and universality of calcium signalling. *Nat Rev Mol Cell Biol* **1**, 11–21 (2000).
2. Montero, M. *et al.* Chromaffin-cell stimulation triggers fast millimolar mitochondrial Ca2+ transients that modulate secretion. *Nat Cell Biol* **2**, 57–61 (2000).
3. Rizzuto, R., De Stefani, D., Raffaello, A. & Mammucari, C. Mitochondria as sensors and regulators of calcium signalling. *Nat Rev Mol Cell Biol* **13**, (2012).
4. Csordás, G., Weaver, D. & Hajnóczky, G. Endoplasmic Reticulum–Mitochondrial Contactology: Structure and Signaling Functions. *Trends Cell Biol* **28**, 523–540 (2018).
5. Denton, R. M. Regulation of mitochondrial dehydrogenases by calcium ions. *Biochim Biophys Acta* **1787**, 1309–1316 (2009).
6. Baumgartner, H. K. *et al.* Calcium elevation in mitochondria is the main Ca2+ requirement for mitochondrial permeability transition pore (mPTP) opening. *J Biol Chem* **284**, 20796–20803 (2009).
7. Garbincius, J. F. & Elrod, J. W. Mitochondrial calcium exchange in physiology and disease. *Physiol Rev* **102**, 893–992 (2022).
8. Bernardi, P. *et al.* Identity, structure, and function of the mitochondrial permeability transition pore: controversies, consensus, recent advances, and future directions. *Cell Death & Differentiation 2023 30:8* **30**, 1869–1885 (2023).
9. Hoth, M., Button, D. C. & Lewis, R. S. Mitochondrial control of calcium-channel gating: a mechanism for sustained signaling and transcriptional activation in T lymphocytes. *Proc Natl Acad Sci U S A* **97**, 10607–10612 (2000).
10. Zeviani, M. & Viscomi, C. Mitochondrial Neurodegeneration. *Cells* **11**, (2022).
11. Zeviani, M. & Carelli, V. Mitochondrial disorders. *Curr Opin Neurol* **20**, 564–71 (2007).
12. Saris, N. E. & Carafoli, E. A historical review of cellular calcium handling, with emphasis on mitochondria. *Biochemistry (Mosc)* **70**, 187–194 (2005).
13. Bernardi, P. Mitochondrial transport of cations: channels, exchangers, and permeability transition. *Physiol Rev* **79**, 1127–1155 (1999).
14. Kamer, K. J. & Mootha, V. K. The molecular era of the mitochondrial calcium uniporter. *Nat Rev Mol Cell Biol* **16**, 545–553 (2015).
15. Palty, R. *et al.* NCLX is an essential component of mitochondrial Na+/Ca2+ exchange. *Proc Natl Acad Sci U S A* **107**, 436–441 (2010).
16. Jiang, D., Zhao, L. & Clapham, D. E. Genome-wide RNAi screen identifies Letm1 as a mitochondrial Ca2+/H+ antiporter. *Science (1979)* **326**, 144–147 (2009).
17. Tsai, M.-F. *et al.* Functional reconstitution of the mitochondrial Ca2+/H+ antiporter Letm1. *J Gen Physiol* **143**, 67–73 (2013).
18. Austin, S. *et al.* TMBIM5 is the Ca2+ /H+ antiporter of mammalian mitochondria. *EMBO Rep* **23**, (2022).

19. Patron, M. *et al.* Regulation of mitochondrial proteostasis by the proton gradient. *EMBO J* **41**, (2022).

20. Nazli, A. *et al.* A mutation in the TMEM65 gene results in mitochondrial myopathy with severe neurological manifestations. *European Journal of Human Genetics 2017 25:6* **25**, 744–751 (2017).

21. De Stefani, D. *et al.* A forty-kilodalton protein of the inner membrane is the mitochondrial calcium uniporter. *Nature* **476**, 336–340 (2011).

22. Sharma, P. *et al.* Evolutionarily conserved intercalated disc protein Tmem65 regulates cardiac conduction and connexin 43 function. *Nat Commun* **6**, (2015).

23. Teng, A. C. T. *et al.* Tmem65 is critical for the structure and function of the intercalated discs in mouse hearts. *Nat Commun* **13**, (2022).

24. Rath, S. *et al.* MitoCarta3.0: An updated mitochondrial proteome now with sub-organelle localization and pathway annotations. *Nucleic Acids Res* **49**, D1541–D1547 (2021).

25. Morgenstern, M. *et al.* Quantitative high-confidence human mitochondrial proteome and its dynamics in cellular context. *Cell Metab* **0**, (2021).

26. Hansen, F. M. *et al.* Mitochondrial phosphoproteomes are functionally specialized across tissues. *bioRxiv* 2022.03.23.485457 (2022) doi:10.1101/2022.03.23.485457.

27. Nishimura, N., Gotoh, T., Oike, Y. & Yano, M. TMEM65 is a mitochondrial inner-membrane protein. *PeerJ* **2**, e349 (2014).

28. Rhee, H. W. *et al.* Proteomic mapping of mitochondria in living cells via spatially restricted enzymatic tagging. *Science (1979)* **339**, 1328–1331 (2013).

29. Tosatto, A., Rizzuto, R. & Mammucari, C. Ca2+ Measurements in Mammalian Cells with Aequorin-based Probes. *Bio Protoc* **7**, (2017).

30. Kim, S. *et al.* Transmembrane glycine zippers: Physiological and pathological roles in membrane proteins. *Proc Natl Acad Sci U S A* **102**, 14278–14283 (2005).

31. Yang, D. *et al.* Short RNA duplexes produced by hydrolysis with Escherichia coli RNase III mediate effective RNA interference in mammalian cells. *Proc Natl Acad Sci U S A* **99**, 9942–9947 (2002).

32. Hill, J. M. M. *et al.* Measuring baseline ca(2+) levels in subcellular compartments using genetically engineered fluorescent indicators. *Methods Enzymol* **543**, 47–72 (2014).

33. Carafoli, E., Tiozzo, R., Lugli, G., Crovetti, F. & Kratzing, C. The release of calcium from heart mitochondria by sodium. *J Mol Cell Cardiol* **6**, 361–371 (1974).

34. Cox, D. A., Conforti, L., Sperelakis, N. & Matlib, M. A. Selectivity of inhibition of Na(+)-Ca2+ exchange of heart mitochondria by benzothiazepine CGP-37157. *J Cardiovasc Pharmacol* **21**, 595–599 (1993).

35. Hernández-SanMiguel, E. *et al.* The mitochondrial Na+/Ca2+ exchanger plays a key role in the control of cytosolic Ca2+ oscillations. *Cell Calcium* **40**, 53–61 (2006).

36. Garbincius, J. F. *et al.* TMEM65 regulates and is required for NCLX-dependent mitochondrial calcium efflux. *Nature Metabolism 2025 7:4* **7**, 714–729 (2025).

ARTICLE IN PRESS

ARTICLE IN PRESS

37. Zhang, J. L. *et al.* TMEM65 functions as the mitochondrial Na+/Ca2+ exchanger. *Nat Cell Biol* **27**, (2025).

38. Sharma, V., Roy, S., Sekler, I. & O'Halloran, D. M. The NCLX-type Na+/Ca2+ Exchanger NCX-9 Is Required for Patterning of Neural Circuits in Caenorhabditis elegans. *J Biol Chem* **292**, 5364–5377 (2017).

39. Eddy, S. R. Accelerated Profile HMM Searches. *PLoS Comput Biol* **7**, e1002195 (2011).

40. Omasits, U., Ahrens, C. H., Müller, S. & Wollscheid, B. Protter: interactive protein feature visualization and integration with experimental proteomic data. *Bioinformatics* **30**, 884–886 (2014).

41. Krogh, A., Larsson, B., Von Heijne, G. & Sonnhammer, E. L. L. Predicting transmembrane protein topology with a hidden Markov model: application to complete genomes. *J Mol Biol* **305**, 567–580 (2001).

42. Savojardo, C., Martelli, P. L., Fariselli, P. & Casadio, R. TPpred3 detects and discriminates mitochondrial and chloroplastic targeting peptides in eukaryotic proteins. *Bioinformatics* **31**, 3269–3275 (2015).

43. Fukasawa, Y. *et al.* MitoFates: improved prediction of mitochondrial targeting sequences and their cleavage sites. *Mol Cell Proteomics* **14**, 1113–1126 (2015).

44. Armenteros, J. J. A. *et al.* Detecting sequence signals in targeting peptides using deep learning. *Life Sci Alliance* **2**, (2019).

45. Lonsdale, J. *et al.* The Genotype-Tissue Expression (GTEx) project. *Nat Genet* **45**, 580–585 (2013).

46. Frezza, C., Cipolat, S. & Scorrano, L. Organelle isolation: functional mitochondria from mouse liver, muscle and cultured fibroblasts. *Nat Protoc* **2**, 287–295 (2007).

47. Schindelin, J. *et al.* Fiji: an open-source platform for biological-image analysis. *Nat Methods* **9**, 676–682 (2012).

48. Granatiero, V., Patron, M., Tosatto, A., Merli, G. & Rizzuto, R. Using targeted variants of aequorin to measure Ca2+ levels in intracellular organelles. *Cold Spring Harb Protoc* **2014**, 86–93 (2014).

49. Granatiero, V., Patron, M., Tosatto, A., Merli, G. & Rizzuto, R. The use of aequorin and its variants for Ca2+ measurements. *Cold Spring Harb Protoc* **2014**, 9–16 (2014).

50. Bonora, M. *et al.* Subcellular calcium measurements in mammalian cells using jellyfish photoprotein aequorin-based probes. *Nat Protoc* **8**, 2105–2118 (2013).

51. Alonso, M. T., Rodríguez-Prados, M., Navas-Navarro, P., Rojo-Ruiz, J. & García-Sancho, J. Using aequorin probes to measure Ca 2+ in intracellular organelles. *Cell Calcium* **64**, 3–11 (2017).

52. Greotti, E. & De Stefani, D. Biosensors for detection of calcium. in *Methods in Cell Biology* vol. 155 337–368 (Academic Press Inc., 2020).

ARTICLE IN PRESS

Acknowledgments

The authors are grateful to Luca Barbato (UniPD) for the help with mutagenesis, Ms. Christiane Bartling-Kirsch (DZNE) and Mr Amal John Mathew (DZNE) for their technical assistance. Moreover, we would like to thank Dr. Christopher E. Hopkins and Dr. Ben Jussila (InVivo Biosystems) for their technical support with CRISPR/Cas9 in C. elegans. This work was supported by grants from the University of Padova (STARS@UNIPD), the Italian Ministry of University and Research (PRIN 2017YF9FBS_002, 2020RRJP5L_002 and PRIN 2020R2BP2E_002), European Union (Next Generation EU CN00000041), the Italian Association for Cancer Research (AIRC 5 per mille 2019 - ID 22759), CARIPARO (ID 59583), CARIPLO, Telethon (GJC21054) and AFM-Telethon (ID ID29104) foundations. DB is a member of: the Deutsche Forschungsgemeinschaft (DFG, German Research Foundation) under Germany's Excellence Strategy – EXC2151 – 390873048, Excellence Cluster ImmunoSensation^2; the ETERNITY project consortium, funded by the European Union through Horizon Europe Marie Skłodowska-Curie Actions Doctoral Networks (MSCA-DN) under the grant number 101072759; the Deutsche Forschungsgemeinschaft (DFG, German Research Foundation) – SPP2453 project number 541647076. BX was supported by a Chinese Scholarship Council (CSC) fellowship (grant number 202108110050). MSH is supported by the ETERNITY project consortium (101072759).

Author contributions

Methodology: **M.V., A.K., E.S., D.B., D.D.S.** Validation: **M.V., L.W., A.K., V.C., B.X., M.S., M.S.H., D.B., D.D.S.** Investigation: **M.V., L.W., A.K., V.C., E.S., B.X., M.S., M.S.H., D.D.S.** Formal analysis: **M.V., L.W., A.K., V.C., E.S., D.B., D.D.S.** Visualization: **L.W., E.S., D.B., D.D.S.** Resources: **D.E.** Funding acquisition: **D.E., R.R., D.B., D.D.S.** Conceptualization: **R.R., D.B., D.D.S.** Writing-Original Draft: **R.R., D.B., D.D.S.** Writing—review and editing: **D.B., D.D.S.** Supervision: **R.R., D.B., D.D.S.** Project administration: **R.R., D.B., D.D.S.**

Competing Interests Statement

All authors declare no competing interests.

ARTICLE IN PRESS

Figure legends

Figure 1. TMEM65 is a conserved protein of the IMM. (a) Cladogram showing the phylogenetic distribution of MCU (red) and TMEM65 (green) homologs across 1088 reference proteomes. (b) Schematic representation of TMEM65 membrane topology. Topological structure was generated using Protter[40]. (c) Western blot showing expression of TMEM65 and TME65-3xFlag in HeLa cells. Comparable results were obtained in at least three independent transfections. (d) Immunolocalization of TMEM65-3xFlag (cyan) and the mitochondrial marker SDHA (magenta) in HeLa cells, scale bar is 10 μm. Comparable staining was obtained in at least three independent transfections and with other mitochondrial markers. (e) Proteinase K protection assay performed in mitoplasts isolated from TMEM65-3xFlag-expressing HeLa cells. Comparable results were obtained in at least three independent experiments.

Figure 2. TMEM65 controls mitochondrial Ca^{2+} homeostasis. (a-b) $[Ca^{2+}]_{mt}$ measurements in HeLa cells expressing a mitochondrially targeted aequorin probe. (a) Representative $[Ca^{2+}]_{mt}$ traces of control, TMEM65 overexpressing and silenced cells. (b) Histograms (mean ± s.d.) of histamine-induced $[Ca^{2+}]_{mt}$ peak values. (c-d) $[Ca^{2+}]_{mt}$ measurements in HeLa cells expressing the mitoGCaMP6 probe. (c) Representative traces of control, TMEM65 overexpressing and silenced cells. (d) Histograms (mean ± s.d.) of mitochondrial Ca^{2+} levels at the indicate time points. Data were analyzed by one-way ANOVA followed by Holm–Sidak's multiple comparisons test. * indicates $p < 0.01$. Individual data points, descriptive statistics and exact p values are included in Source Data Table.

Figure 3. TMEM65 mediates Na^+-dependent mitochondrial Ca^{2+} efflux. (a-d) $[Ca^{2+}]_{mt}$ measurements in digitonin-permeabilized HeLa cells. (a-b) Representative $[Ca^{2+}]_{mt}$ traces of control, TMEM65 overexpressing and silenced cells in the absence (a) or presence (b) of 10 mM Na^+. (c-d) Histograms (mean ± s.d.) of maximal Na^+-independent (c) and Na^+-dependent (d) mitochondrial Ca^{2+} influx and efflux rates. Data were analyzed by one-way ANOVA followed by Holm–Sidak's multiple comparisons test. * indicates $p < 0.05$. (e-g) $[Ca^{2+}]_{mt}$ measurements in control and TMEM65 overexpressing intact HeLa cells treated with either vehicle (DMSO) or 20 μM CGP-37157. (e) Representative $[Ca^{2+}]_{mt}$ traces. (f) Histograms (mean ± s.d.) of histamine-induced $[Ca^{2+}]_{mt}$ peak values. (g) Histograms (mean ± s.d.) of normalized mitochondrial Ca^{2+} efflux. Data were analyzed by two-way ANOVA followed by Holm–Sidak's multiple comparisons test. * indicates $p < 0.001$, ns=not significant. Individual data points, descriptive statistics and exact *p* values are included in Source Data Table.

Figure 4. TMEM65-dependent Ca^{2+} efflux is independent of NCLX expression. (a-e) $[Ca^{2+}]_{mt}$ measurements in intact HeLa cells expressing an aequorin-based probe. (a) Representative $[Ca^{2+}]_{mt}$ traces showing the effect of TMEM65 overexpression in control and NCLX-silenced cells. (b) Histograms (mean ± s.d.) of histamine-induced $[Ca^{2+}]_{mt}$ peak values. Where indicated, cells were treated with 20 μM CGP-37157. Data were analyzed by three-way ANOVA followed by Holm–Sidak's multiple comparisons test. * indicates $p < 0.01$. (c) Representative $[Ca^{2+}]_{mt}$ traces showing the effect of TMEM65 overexpression in control and NCLX-KO cells. (d) Histograms (mean ± s.d.) of histamine-induced $[Ca^{2+}]_{mt}$ peak values. Data were analyzed by two-way ANOVA followed by Holm–Sidak's multiple comparisons test. * indicates $p < 0.001$. (e) Histograms (mean ± s.d.) of normalized mitochondrial Ca^{2+} extrusion rate. Data were analyzed by two-way ANOVA followed by Holm–Sidak's multiple comparisons test. * indicates $p < 0.001$. (f-g) $[Ca^{2+}]_{mt}$ measurements in digitonin-permeabilized HeLa cells. (f) Representative $[Ca^{2+}]_{mt}$ traces showing

the effect of TMEM65 overexpression in control and NCLX-KO cells. (g) Histograms (mean ± s.d.) of maximal Na^+-dependent mitochondrial Ca^{2+} efflux rates. Data were analyzed by two-way ANOVA followed by Holm–Sidak's multiple comparisons test. * indicates $p < 0.001$. Individual data points, descriptive statistics and exact *p* values are included in Source Data Table.

Figure 5. Loss of CeTMEM65 is detrimental for embryos development. (a) BLAST analysis of human TMEM65 against the *C. elegans* WormBase database. The figure shows the hits ranked by sequence similarity. Below, the sequence alignments of human TMEM65 (Hs TMEM65, in blue) vs *C. elegans* TAG-321 (Ce TAG-321, green) and C03B8.3 (Ce C03B8.3, red). (b) AlphaFold-predicted structures of human TMEM65 and *C. elegans* orthologs. The models highlight domains with conserved fold and organization. (c) Hatching assay of wt (grey), *tag-321(bon103)* (green), *C03B8.3(bon104)* (red) and *C03B8.3(bon104);tag-321(bon103)* (blue) grown at 20°C. (d-e) Lifespan assays at (d) 20°C and (e) 25°C. The means (±SEM) of the median survival are reported below the graphs. Genotypes are indicated by colored dashes. (f) Schematic representation of the hatching assay. Created in BioRender. Bano, D. (2025) https://BioRender.com/asudllh (g) Hatching assay of wt (grey), *tag-321(bon103*) (green), *C03B8.3(bon104)* (red) and *C03B8.3(bon104);tag-321(bon103)* (blue) larvae from eggs incubated at 25°C. (h) Representative DIC images of eggs extracted from gravid adult animals and maintained at 25°C. Yellow arrowhead indicates a vacuole. (i) Schematic representation of mitochondrial Ca^{2+} transport. Genetic inhibition results in MCU complex and TMEM65 loss (as grey cartoons). Created in BioRender. Bano, D. (2025) https://BioRender.com/asudllh (j) Representative DIC images of eggs that were extracted from gravid adult animals and maintained at 25°C. Yellow arrowhead indicates a vacuole. (k) Hatching assay of wt, *C03B8.3(bon104);tag-321(bon103)* and *C03B8.3(bon104);mcu-1(ju1154);tag-321(bon105)* at 25°C. (l) Schematic representation of a population-based hatching assay paradigm. Created in BioRender. Bano, D. (2025) https://BioRender.com/asudllh (m) Hatching assay of wt, *C03B8.3(bon104);tag-321(bon103)* and *C03B8.3(bon104);mcu-1(ju1154);tag-321(bon105)* at 25°C using the paradigm described in (5l). (n) Hatching assay of wt, *tag-321(bon103)* and *C03B8.3(bon104)* at 25°C using the paradigm described in (5l). (o) Schematic representation of NCLX genetic inhibition. Created in BioRender. Bano, D. (2025) https://BioRender.com/asudllh (p) Hatching assay of wt, *ncx-9(gk234237)* and *ncx-9(gk773708)* at 25°C using the paradigm described in (5l). All data are presented as mean ± s.d., unless otherwise specified. Data from panels c, g, k, m and n were analyzed by one-way ANOVA followed by Holm–Sidak's multiple comparisons test. Data from panel p were analyzed using an unpaired two-sample t-test. **p<0.01, ****p<0.0001, ns=not significant. Individual data points, descriptive statistics and exact *p* values are included in Source Data Table.

ARTICLE IN PRESS

TMEM65 drives Na+ -dependent mitochondrial Ca^{2+} efflux, independently of NCLX. Its dysfunction causes increased sensitivity to mild stress and links mitochondrial Ca^{2+} overload to degeneration.

ARTICLE IN PRESS

Peer Review Information: *Nature Communications* thanks Elizabeth Jonas, and the other, anonymous, reviewer(s) for their contribution to the peer review of this work. A peer review file is available.

ARTICLE IN PRESS

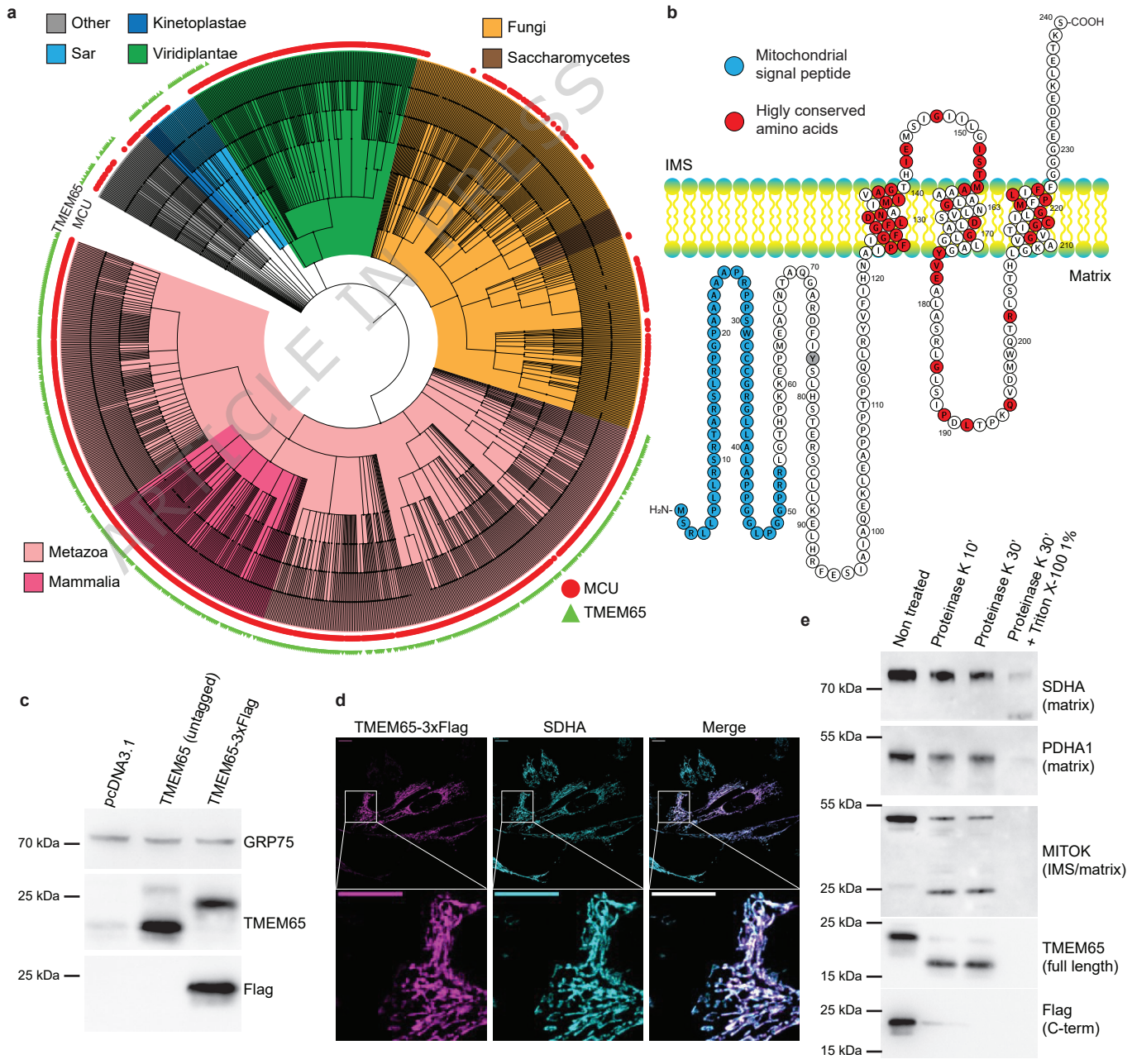
a
Other
Kinetoplastae
Sar
Viridiplantae
Fungi
Saccharomycetes
TMEM65
MCU
Metazoa
Mammalia
MCU
TMEM65
b
Mitochondrial signal peptide
Higly conserved amino acids
IMS
Matrix
H2N-
-COOH
c
pcDNA3.1
TMEM65 (untagged)
TMEM65-3xFlag
70 kDa
GRP75
25 kDa
TMEM65
25 kDa
Flag
d
TMEM65-3xFlag
SDHA
Merge
e
Non treated
Proteinase K 10'
Proteinase K 30'
Proteinase K 30' + Triton X-100 1%
70 kDa
SDHA (matrix)
55 kDa
PDHA1 (matrix)
55 kDa
MITOK (IMS/matrix)
25 kDa
25 kDa
TMEM65 (full length)
15 kDa
25 kDa
Flag (C-term)
15 kDa

ARTICLE IN PRESS

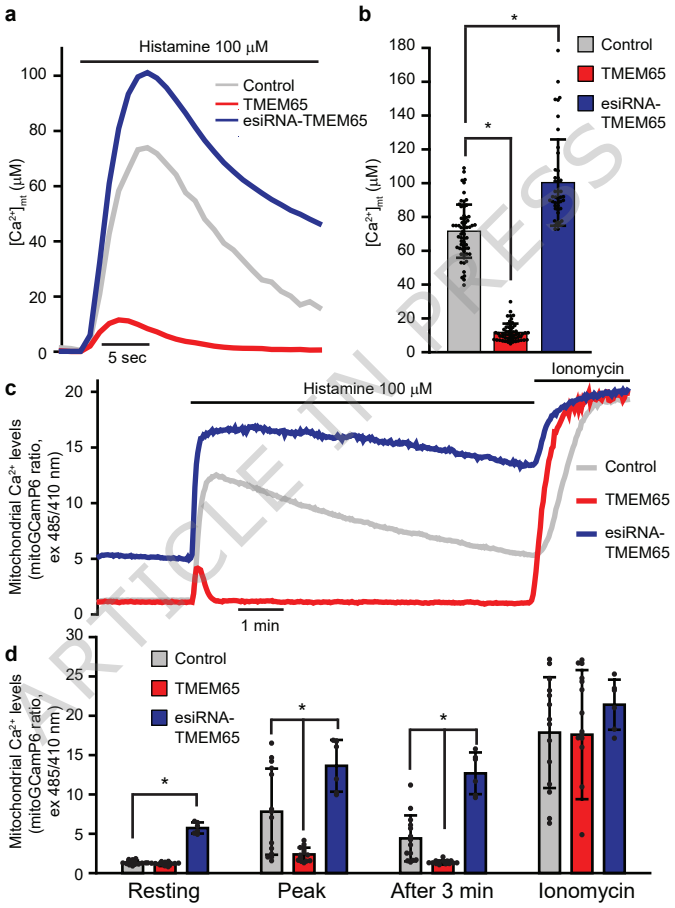

ARTICLE IN PRESS

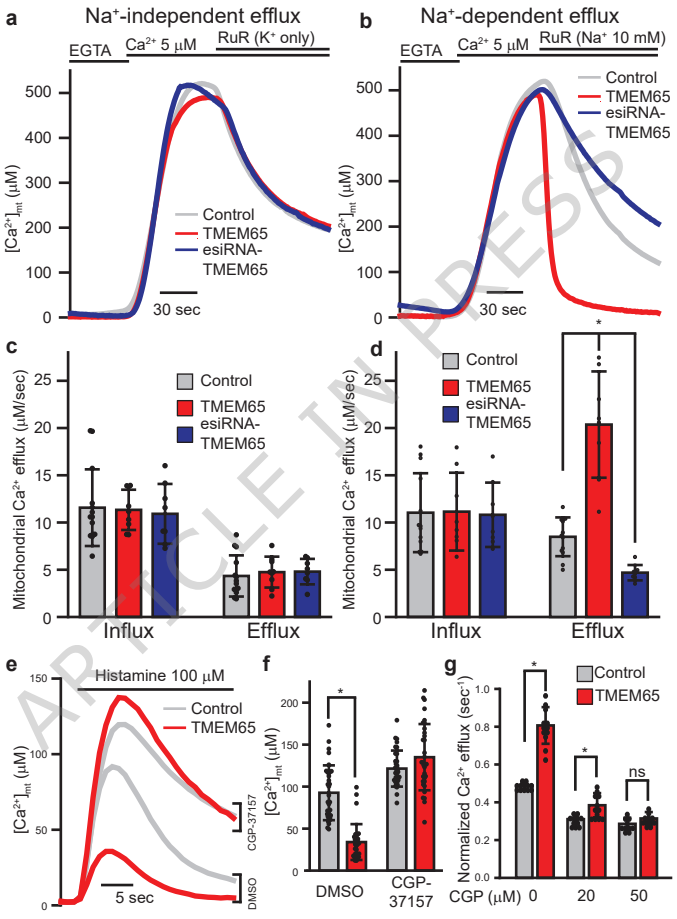

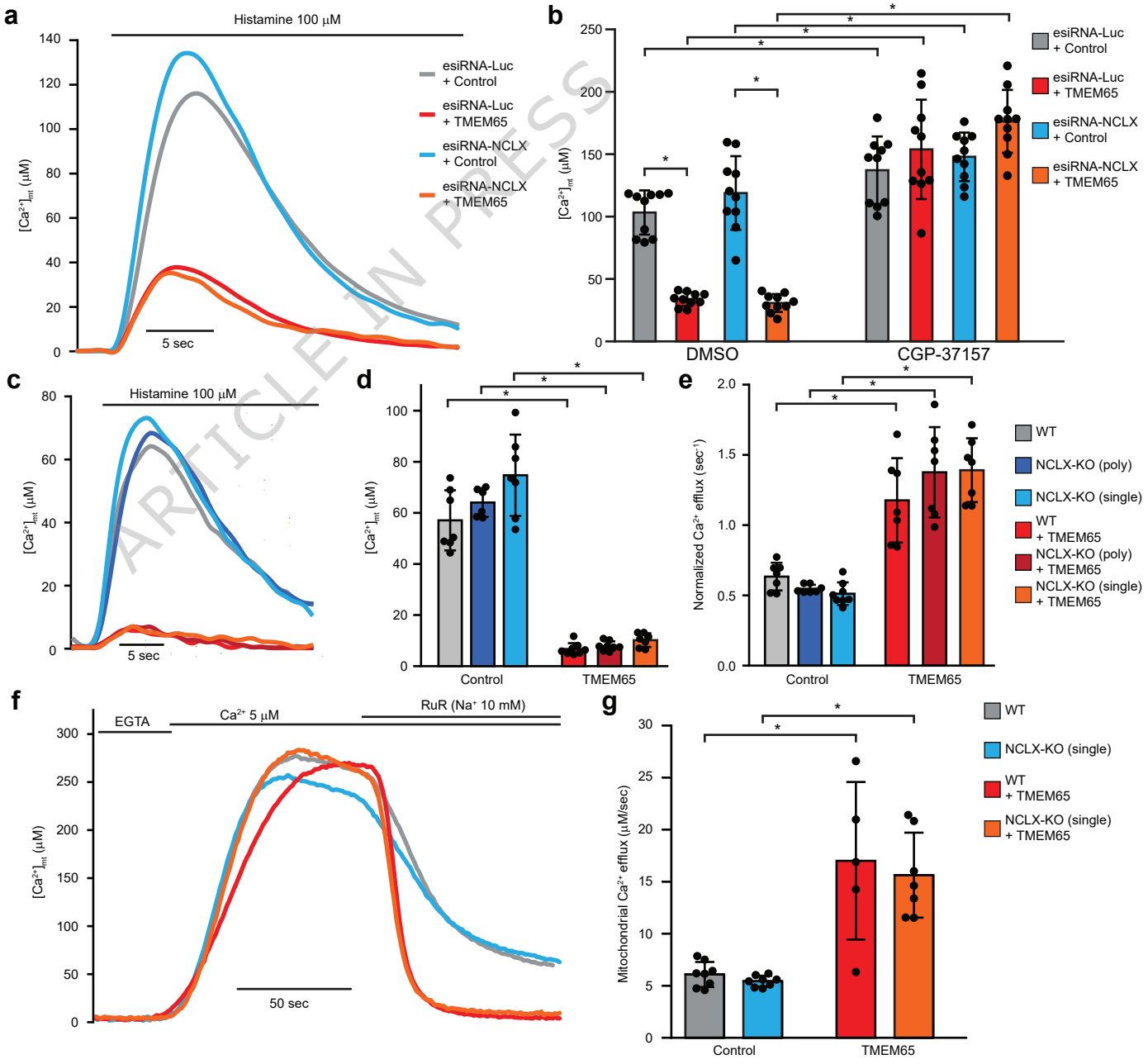

ARTICLE IN PRESS

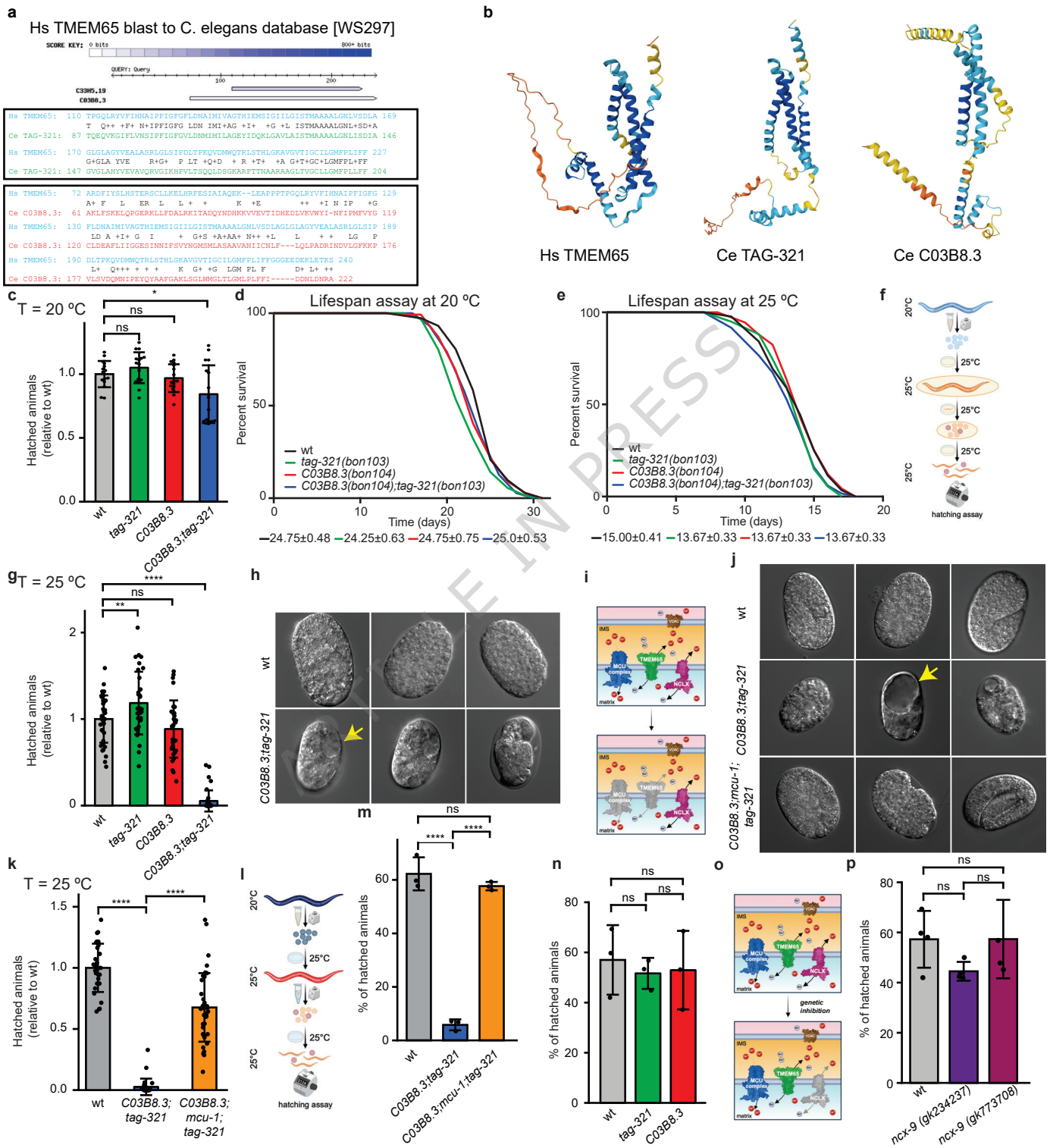
a
Hs TMEM65 blast to C. elegans database [WS297]
b
Hs TMEM65
Ce TAG-321
Ce C03B8.3
c
T = 20 ºC
Hatched animals (relative to wt)
wt
tag-321
C03B8.3
C03B8.3;tag-321
d
Lifespan assay at 20 ºC
Percent survival
Time (days)
wt
tag-321(bon103)
C03B8.3(bon104)
C03B8.3(bon104);tag-321(bon103)
24.75±0.48 24.25±0.63 24.75±0.75 25.0±0.53
e
Lifespan assay at 25 ºC
15.00±0.41 13.67±0.33 13.67±0.33 13.67±0.33
f
hatching assay
g
T = 25 ºC
h
i
j
C03B8.3;mcu-1; tag-321
k
T = 25 ºC
C03B8.3; tag-321
C03B8.3; mcu-1; tag-321
l
hatching assay
m
% of hatched animals
C03B8.3;mcu-1;tag-321
n
o
genetic inhibition
p
ncx-9 (gk234237)
ncx-9 (gk773708)